ACS Photonics

pubs.acs.org/journal/apchd5 Article

Multifunctional Spaceplates for Optical Aberration Correction

Published as part of ACS Photonics virtual special issue "Frontiers and Applications of Plasmonics and Nanophotonics".

Yixuan Shao, Robert Lupoiu, Jiaqi Jiang, You Zhou, Tom D. Milster, and Jonathan A. Fan*

Cite This: *ACS Photonics* 2024, 11, 1753−1760 Read Online

ACCESS | Metrics & More | Article Recommendations | Supporting Information

ABSTRACT: Spaceplates are nonlocal optical devices with the potential to reduce the form factor of optical systems, but current implementations are limited in performance and ability to correct for optical aberrations. We introduce a new class of multifunctional spaceplates, designed using gradient-based freeform optimization, which exhibit exceptional efficiencies, compression ratios, and aberration correcting capabilities. We show that such spaceplates can serve as correctors for metasurfaces and refractive optical elements, and we demonstrate that multifunctional spaceplates can extend to support multispectral, Petzval field curvature, and spherical aberration correction. We anticipate that these spaceplate concepts will enable the realization of ultracompact optical systems.

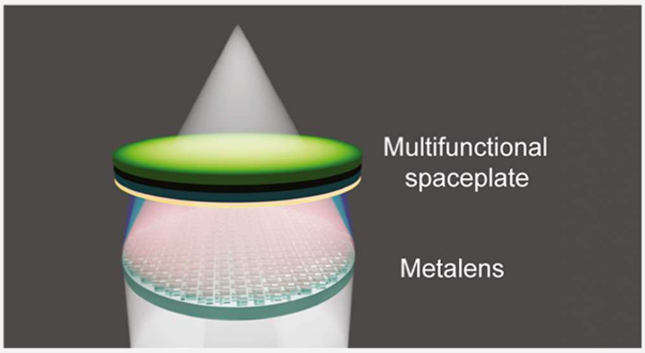

KEYWORDS: *spaceplates, flat optics, thin-film optics, aberration, imaging system, nanophotonics*

■ INTRODUCTION

Over the last two decades, extensive research has been devoted to the development of nano-optical imaging systems with reduced size and weight.[1] A major focus has been at the device level, where optical metasurfaces have been developed that seek to substitute traditional bulky optics with nanostructured thin films.[2−10] Metasurfaces can be designed to exhibit a broad range of amplitude and phase responses, leading to gratings, lenses, and holographic surfaces featuring new regimes of spectral[11−14] and polarization control.[15−18] A more recent development has been the reduction of the separation distances between optical components using spaceplates (Figure 1a), which are volumetric nonlocal optical devices that can emulate the optical responses of free space within a reduced physical space.[19−24] Concepts such as the spaceplate are ultimately required to enable reductions in total optical system size while retaining image fidelity and spectral range.

While such nanophotonic-enabled optical systems have great potential, current embodiments of these systems suffer from various aberrations that make their practical implementation challenging. Much attention has been placed on correcting aberrations in metasurfaces, where chromatic aberrations have been addressed through dispersion engineering,[25−30] and monochromatic aberrations have been addressed through the codesign of multi-metasurface systems.[31−34] However, relatively little work has been done regarding aberration corrections in spaceplates or the potential role of spaceplates in correcting for aberrations, where current designs are restricted to a single wavelength and relatively small thicknesses and numerical apertures. Extensions of the spaceplate concept to devices that can address chromatic and monochromatic aberrations can lead to enhanced optical systems with new form factors and capabilities. Spaceplates are particularly well suited for aberration correction because they are volumetric nonlocal devices and can have sufficient thickness to address limitations posed by overlapping nonlocality when performing aberration correction.[35]

In this study, we present a generalized framework for multifunctional spaceplates based on thin-film dielectric stacks, which can compress space as a function of incidence wavelength and angle. To design these devices, we developed a novel gradient-based optimization algorithm in which the thickness and refractive index of each dielectric layer are free parameters for design. Benchmarking with conventional spaceplate concepts indicates that our devices yield unprecedented compression factors and numerical apertures. We show that these spaceplates can be independently configured for a set of wavelengths (Figure 1b) and serve as a chromatic

Received: January 16, 2024
Revised: March 7, 2024
Accepted: March 8, 2024
Published: March 20, 2024

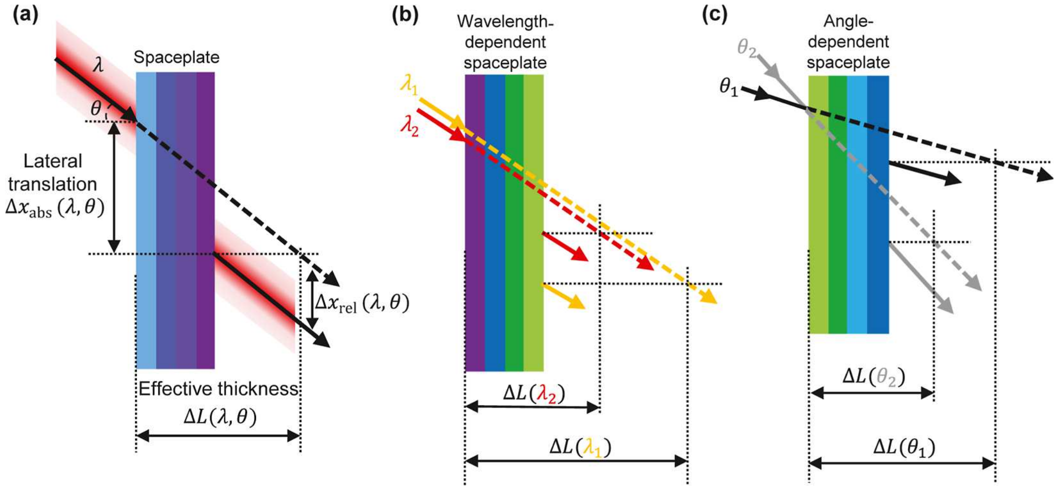

Figure 1. Multifunctional spaceplates based on multilayer dielectric thin-film stacks. (a) Multifunctional spaceplate mimics an air gap with an effective thickness (ΔL) that is a function of the wavelength, λ, and incidence angle, θ, of an incident beam. Equivalently, the spaceplate serves to laterally shift the incident beam by Δx_{abs} as a function of λ and θ. The thick solid lines depict the actual beam paths with the spaceplate, while the thick dashed lines represent free-space beam propagation without the spaceplate. (b) Multifunctional spaceplate can correct for chromatic aberrations by compressing space as a function of wavelength. (c) Multifunctional spaceplate can correct for certain monochromatic aberrations by arbitrarily specifying lateral beam shifts as a function of θ, leading to angle-dependent compression of space.

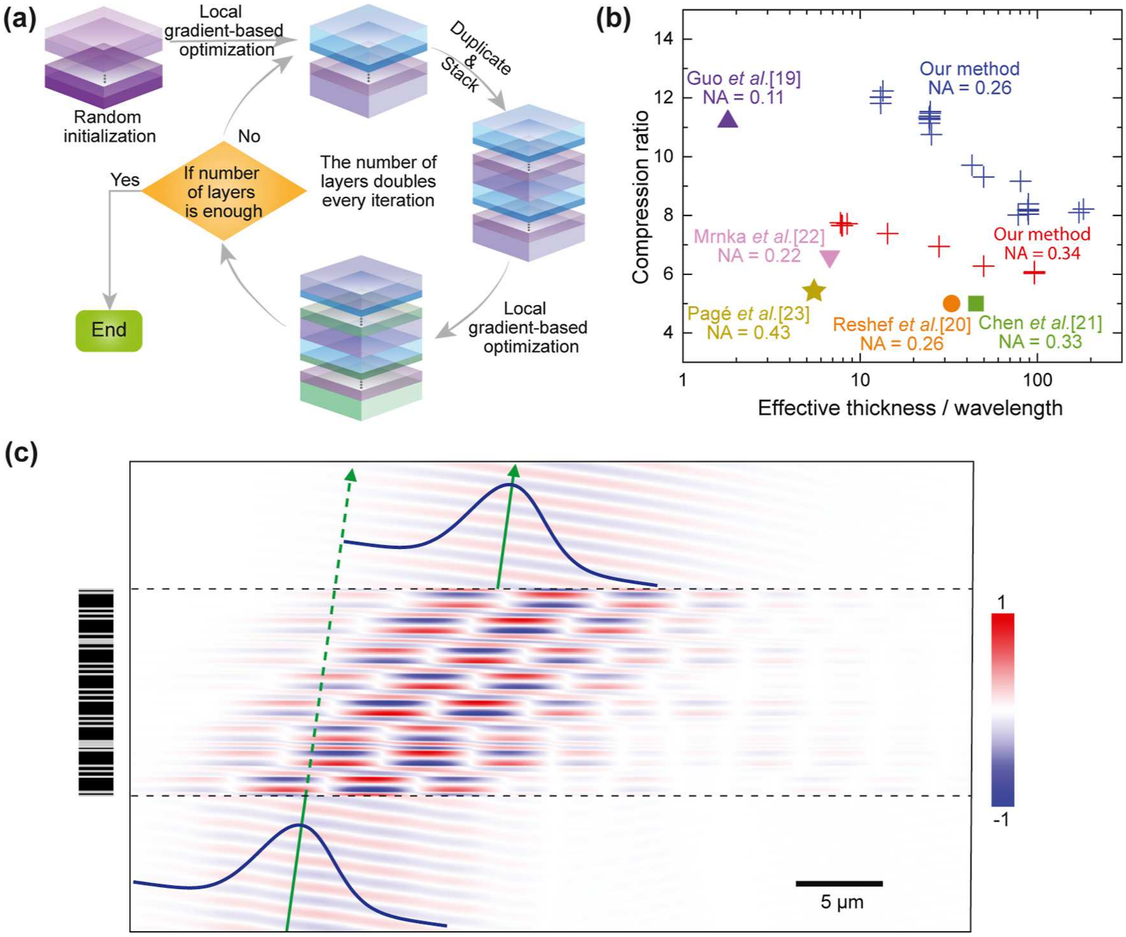

Figure 2. Our spaceplate optimization algorithm. (a) Flowchart of the optimization algorithm. We start with a few-layered structure with randomly initialized thicknesses and refractive indices. We then gradient-optimize the structure, duplicate, and vertically stack the structure to double the device thickness and repeat until the desired number of layers is achieved. (b) Scatter plot of the compression ratios and effective thicknesses of optimized classical spaceplates produced by our algorithm and from previous works. (c) Plot of the H_z field from an FDTD simulation of a representative optimized spaceplate. The incident Gaussian beam is obliquely incident on the structure with an 8° angle from normal, and the lateral translation of the outgoing beam is indicated.

aberration corrector for metasurface and refractive optics. We further show that spaceplates featuring effective air gaps as an arbitrary function of the incidence angle (Figure 1c) can be used to correct for Petzval field curvature and spherical aberration, indicating the vast potential of hybrid optical systems that combine nanophotonic and bulk optical elements.

■ METHODS

To frame our spaceplate design methodology in the context of aberration correction, we first present an interpretation of the spaceplate functionality based on the lateral translation of incident rays. While this interpretation is equivalent to that of air gap compression, it provides a more direct physical explanation of how spaceplates can correct for aberrations. In this picture, we model the rays with wavelength λ as a Gaussian beam with finite width. Assuming that the Gaussian beam has a small beam angular spectrum range and a uniform transmittance $|t|^2$, the spaceplate-transfer function $H(\theta)$ for a given incidence angle θ can be approximated as

$$H(\theta) = |t|e^{i\phi(\theta)} = |t|\exp\left(i\phi(\theta_{\text{in}}) + i\frac{d\phi}{d\theta_{\text{in}}}(\theta - \theta_{\text{in}})\right) \tag{1}$$

where $\phi(\theta)$ is the phase response of the structure. The absolute lateral shift of the center of the beam, Δx_{abs} (Figure 1a), is then

$$\Delta x_{\text{abs}}(\theta_{\text{in}}, \lambda) = -\frac{\lambda}{2\pi\cos(\theta_{\text{in}})}\frac{d\phi}{d\theta_{\text{in}}} \tag{2}$$

A derivation of this expression is given in the Supporting Information. Due to the symmetry of our thin-film stack system and our use of isotropic materials with positive dielectric constant, Δx_{abs} is necessarily a positive number. On the other hand, the shift of the beam exiting the spaceplate of thickness L relative to a ray propagating through free space of the same thickness, $\Delta x_{\text{rel}} = \Delta x_{\text{abs}} - L\tan(\theta_{\text{in}})$, can be positive or negative. These shifts correspond to spaceplate compression or expansion of free space, respectively, and both types of shifts are required when considering the use of spaceplates for certain types of aberration corrections, as we will see later.

To demonstrate the validity of our lateral shift expression, we consider the classical monochromatic spaceplate that mimics a constant air gap, L_{eff}, which we term its effective thickness. Its transfer function is

$$H_{\text{Air}}(\theta; L_{\text{eff}}) = \exp\left(i\frac{2\pi}{\lambda}L_{\text{eff}}\cos\theta\right) \tag{3}$$

Substituting this transfer function into eq 2 produces the lateral shift $\Delta x_{\text{Air}}(\theta_{\text{in}}, \lambda) = L_{\text{eff}}\tan(\theta_{\text{in}})$, which matches a simple geometric optics picture that considers a ray propagating through an air gap with a thickness of L_{eff}.

Our approach for specifying the targeted spaceplate response for both classical and multifunctional spaceplates, given a desired $\Delta x(\theta_{\text{in}})$, is now clear. Equation 2 can be directly integrated to produce an incident-angle-dependent spaceplate phase response

$$\phi(\theta_{\text{in}}) = -\frac{2\pi}{\lambda}\int_0^{\theta_{\text{in}}}\Delta x(\theta)\cos(\theta)d\theta + \text{Const} \tag{4}$$

For spaceplates designed to address chromatic responses, the term Δx can be a function of wavelength as well as θ_{in} without any loss of generality. In general, the phase function calculated from eq 4 may not always be physically realizable because the desired shift amount Δx can be negative. However, we can circumvent this issue by increasing the effective thickness of the spaceplate by a constant to constrain the solution space to physically achievable geometries. More details are in the Supporting Information.

Next, we minimize the difference between the actual phase response and the required phase response by optimizing the thicknesses and refractive indices of the multilayer structure. We propose the algorithm depicted in Figure 2a. Mechanistically, we start with a randomly initialized ten-layer device "seed" and perform local gradient-based optimization on the device using the nonlinear conjugate gradient method.[36] During this iterative optimization process, the device is simulated using the transfer matrix method (TMM), and local gradients are calculated by autodifferentiating the TMM expressions. Analytic TMM autodifferentiation has been previously used for various thin-film stack design tasks and provides a straightforward way to calculate gradients in high-dimensional optimization landscapes.[37,38] Once the initial thin-film stack is optimized, it is duplicated, vertically stacked, and used as a starting point for further local gradient-based optimization. These duplication, stacking, and local optimization steps are repeated until the desired number of layers is achieved. Due to the nonconvex nature of the optimization landscape,[23] multiple local optima exist, and we therefore perform optimization on 1000 random device seeds in parallel and select the best overall performing final device.

Compared to alternative design concepts,[20,23] our cyclic device stacking and optimization algorithm is particularly effective and computationally efficient for spaceplate optimization for two reasons. First, given a spaceplate that perfectly mimics an air gap, the stacking of two such spaceplates will mimic an air gap with twice the gap thickness. As such, detailed designs of high-performing thin spaceplates can and should be used to design relatively thick spaceplates. Our need for further gradient-based optimization after each stacking step is due to the fact that our spaceplates do not perfectly mimic air gaps, and optical interactions between spaceplates will manifest upon vertical stacking. Second, the optimization landscapes of thin spaceplates are exponentially smaller than those of thick spaceplates, making the gradient-based search for promising thin devices computationally tractable and efficient. With detailed results included in the Supporting Information, we show that our optimization algorithm performs better than optimizing a very thick spaceplate directly without the duplicating and stacking cycles.

■ RESULTS

We first focus on the application of our cyclic design algorithm on classical monochromatic spaceplates, which enables proper benchmarking with prior studies. We consider spaceplates that operate with TM polarization, a wavelength of 1.55 μm, and refractive indices that continuously range from 1.0 to 3.45. To perform this design task, we consider the following Figure of Merit (FoM)

$$\text{FoM} = -\frac{R^3}{(C + \Delta\phi)^2} \tag{5}$$

Here, R is the compression ratio, $\Delta\phi$ is the root-mean-square phase error, and C is a constant to avoid a zero denominator. The denominator minimizes the difference between the actual

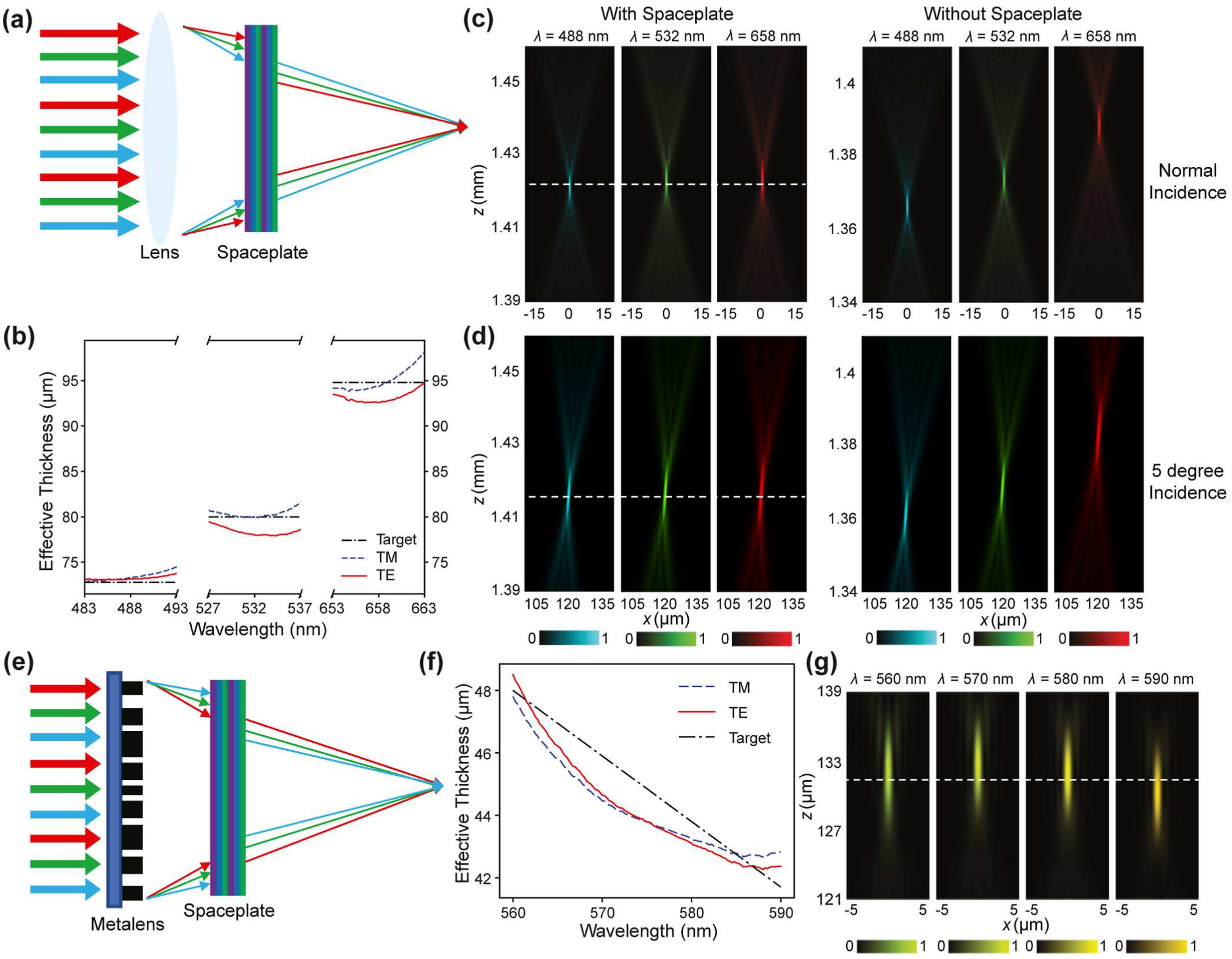

Figure 3. Multifunctional spaceplate design for chromatic aberration correction. (a) Schematic of a multifunctional spaceplate that corrects for chromatic aberration from a refractive lens. (b) Plot of the optimized multifunctional spaceplate's effective thickness as a function of wavelength for the refractive optical system. (c) Simulated light intensity profile at the focal plane for a plane wave incident on a refractive lens (NA = 0.34), with and without a spaceplate. (d) Simulated light intensity profile at the focal plane of a plane wave with five-degree oblique incidence on a refractive lens (NA = 0.26), with and without a spaceplate. (e) Schematic of a multifunctional spaceplate that corrects for chromatic aberration from a metalens (NA = 0.34). (f) Plot of the optimized multifunctional spaceplate's effective thickness as a function of wavelength for the metalens system. (g) Simulated light intensity profile at the focal plane for a plane wave incident on the metalens−spaceplate system.

and desired spaceplate phase response as a function of incidence angle so that the device functions as close as possible to that of an equivalent air gap. The range of incidence angles covered in the FoM is specified to span a numerical aperture (NA) of the interest. The numerator maximizes the compression ratio, which is defined as the ratio of the effective thickness to the actual thickness of the spaceplate and enables maximal shrinkage of an optical system. A range of one to five stacking and optimization cycles (Figure 2a) are performed to produce a range of final devices with thicknesses that span 1.55−35 μm, indicating the potential of our cyclic design algorithm to readily produce spaceplates with a wide range of effective thicknesses.

The compression ratios and effective thicknesses of devices designed using our algorithm, together with benchmark results from prior studies optimized using a similar FoM, are shown in Figure 2b. Compared with benchmark devices with similar NAs, our devices feature larger combinations of compression ratios and effective thicknesses. In general, the compression ratios of our devices reduce relatively slowly as the effective thickness increases, indicating the efficacy of our cyclic design algorithm to enhance the device thickness while maintaining high compression ratios. Our thickest devices feature 320 total layers and an effective thickness of 265.8 μm, indicating the potential utility of spaceplates in macroscopic optical systems. A frequency domain simulation of a Gaussian beam incident on a representative spaceplate is presented in Figure 2c and visualizes the lateral beam displacement functionality of the spaceplate. The nearly matching spatial profiles of the incident and outgoing Gaussian beams, together with a Δx_{abs} that matches the value calculated using eq 2, indicates that the spaceplate phase response closely matches the desired transfer function for air gap compression. The strong fields visualized within the spaceplate indicate the device's use of multiple strong nonlocal optical interactions, in the form of internal reflections, to elongate the effective propagation distance of the beam. We point out that the strong internal reflections, however, depend heavily on the accurate implementation of

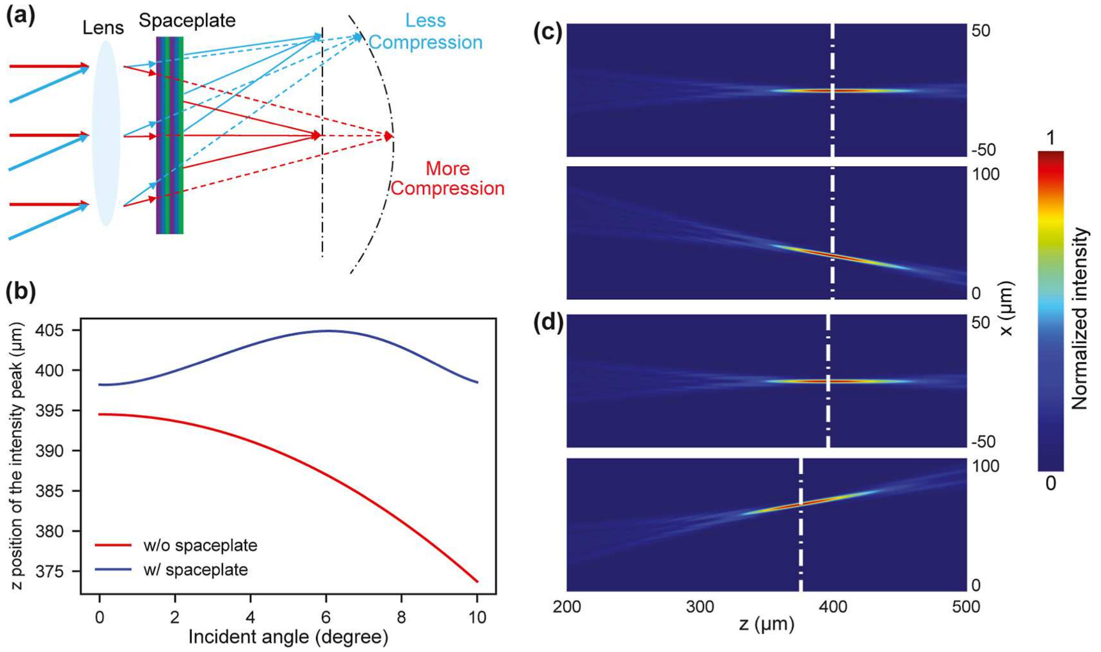

Figure 4. Multifunctional spaceplate design for Petzval field curvature correction. (a) Schematic of Petzval field curvature correction using a multifunctional spaceplate, which is designed to compress more space for small-angle rays and less space for large-angle rays. Solid lines and dashed lines correspond to rays in the cases with and without the spaceplate, respectively. (b) Plot of the position of the simulated intensity peak as a function of the field angle with and without the spaceplate. (c,d) Simulated light intensity profile with a plane wave incident on the refractive lens, followed by the designed spaceplate for the on-axis and 10° off-axis field with (c) and without (d) the spaceplate. The white dotted lines show the focal plane.

phase accumulation to ensure constructive interference, which renders the structure notably susceptible to fabrication errors. In the Supporting Information, we include a perturbation analysis of the example spaceplate from Figure 2c.

We next extend our spaceplate analysis to multifunctional aberration-correcting spaceplates. In all aberration correction demonstrations, we design polarization-independent spaceplates to ensure their capability to operate in three-dimensional imaging systems. We first focus on devices capable of correcting chromatic aberration from refractive and metasurface lenses (Figure 3a). For our refractive lens demonstration, we interface spaceplates with a singlet BK7 glass refractive and tailor our spaceplate for red (653−663 nm), green (527−537 nm), and blue (483−493 nm) wavelengths. The BK7 lens features focal planes for red light that are approximately 22 μm further from that of blue light, and correcting for these aberrations requires a multifunctional spaceplate featuring an effective thickness of 95 μm for red wavelengths, 80 μm for green wavelengths, and 73 μm for blue wavelengths (Figure 3b). Compared to the conventional spaceplates shown in Figure 2, these devices are polarization independent, have high transmittance explicitly enforced in the FoM (details are in the Supporting Information), and contain refractive indices constrained to the range of 1.46−3.3.

We optimized 1000 devices with random seed structures and performed six stacking and optimization cycles to produce final devices comprising 640 thin-film layers. The target device NA is 0.34. The highest performing device is 128 μm thick and supports an average transmittance of 94% over the working wavelength bands. To simulate the combined refractive lens and spaceplate system, we utilize a hybrid modeling approach in which the lens is simulated with ray tracing, the transmitted rays are converted to a wavefront according to their optical path lengths, the planewave-spaceplate response for each plane wave mode is calculated using TMM, and the transmitted plane waves are summed together (more details are in the Supporting Information Section). The resulting focal planes for a refractive lens (NA = 0.34) and normally incident light, with and without the spaceplate, are shown in Figure 3c, and related plots for a refractive lens (NA = 0.26) and 5° oblique light incidence are shown in Figure 3d. In both cases, the inclusion of the spaceplate shows qualitative improvements in chromatic aberration correction and light focusing to a single focal plane.

In a second chromatic aberration demonstration, we show that spaceplates can perform chromatic correction for metalenses (Figure 3e). In this example, we consider a metalens with an NA of 0.34 operating from 560 to 590 nm, which is roughly the bandwidth of a light-emitting diode and for which considerable chromatic aberration is observed with the metalens. The desired spaceplate effective thickness versus wavelength to correct for the metalens aberration is plotted in Figure 3f together with the response of our optimized physical devices, indicating good convergence between the desired and actual effective thickness profiles for both polarizations of light. The hybrid metalens−spaceplate system is simulated using a combination of finite difference time domain simulations for the metalens and TMM for the spaceplate (more details are in the Supporting Information section), and the light intensity profiles at the cross-section plane for normally incident waves are visualized in Figure 3g and show light focusing to the focal plane across the bandwidth of interest (reference focusing profiles without the spaceplate are in the Supporting Information section).

We next examine the potential for multifunctional spaceplates to address monochromatic aberrations and show that a spaceplate can correct Petzval field curvature aberrations from

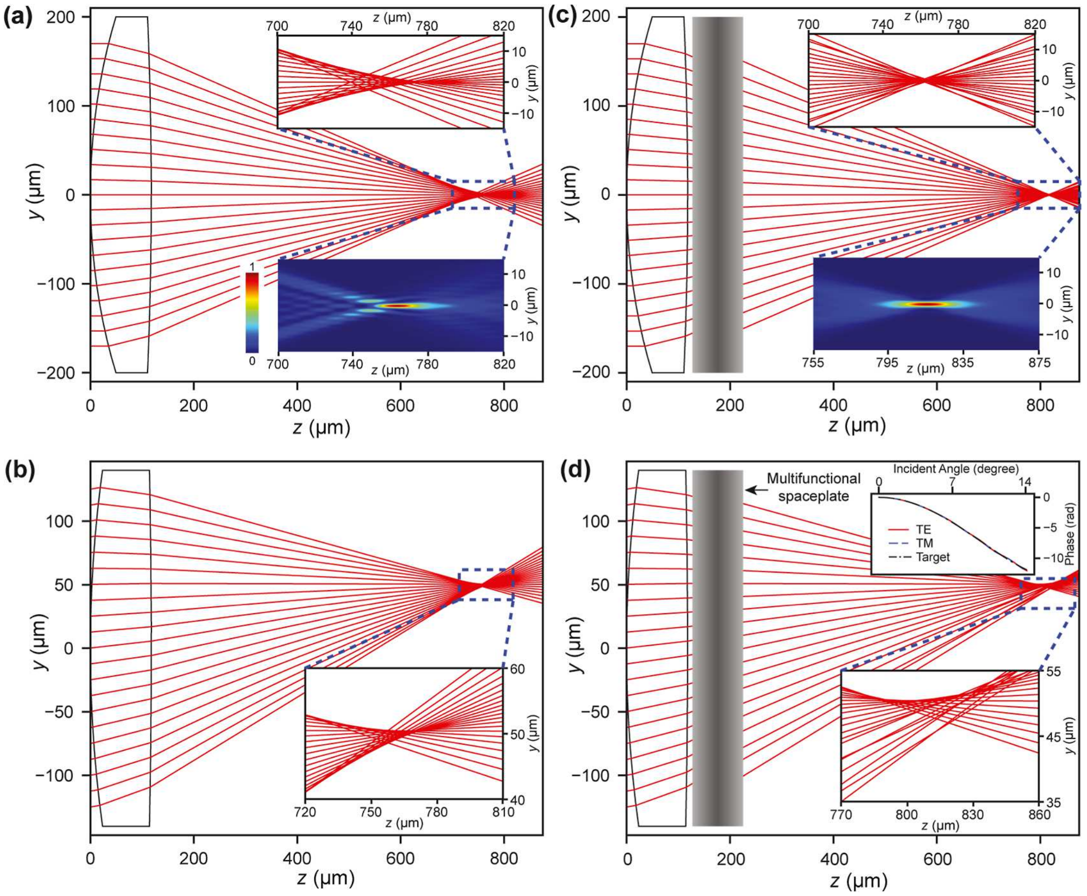

Figure 5. Multifunctional spaceplates for spherical aberration correction. (a,b) Ray tracing diagrams of (a) normal and (b) off-axis incident rays propagating through a spherical lens. Off-axis illumination is performed at a 4° angle. (c,d) Ray tracing diagrams of (c) normal and (d) off-axis incident rays propagating through a hybrid spherical-lens−spaceplate system. Insets: Zoomed-in view of the focal point region in terms of rays and waves. Upper inset of (d): the targeted and actual phase response of the spaceplate.

a biaspheric singlet. The concept is illustrated in Figure 4a and shows that the Petzval field curvature from the singlet produces a curved focal plane (dashed red and blue lines). To enable focusing to a flat focal plane (solid red and blue lines), the spaceplate is designed to compress the air gap by different amounts as a function of incidence angle such that the focal point of the on-axis field shifts more toward the lens compared to that of the off-axis field.

We calculate the focusing intensity position and profile of the imaging system with and without the spaceplate for different incident fields using the same ray tracing-TMM simulation method discussed earlier. Figure 4b shows the position of the intensity peak as a function of the incidence angle. Without the spaceplate, the focal point shifts by 21 μm as the incident angle changes from 0 to 10°, but with the optimized spaceplate design, the shifts are within a 7 μm range. Figure 4c,d shows the intensity profile of the system with and without the spaceplate for the on-axis field and 10° off-axis field, showing that the spaceplate serves to align the peak intensity along the focal plane.

Finally, we show that a multifunctional spaceplate can be used to correct for spherical aberration from a spherical BK7 lens. Spherical aberration can be visualized in the on- and off-axis ray tracing diagrams in Figure 5a,b, respectively, for a spherical lens with an aperture diameter of 340 μm for the on-axis case and 250 μm for the off-axis case and an operating wavelength of 630 nm. Zoomed-in views around the focal point (insets in Figure 5a,b) show that rays entering the lens near its edge are focused at a closer point than rays entering near the center, producing a classic focus profile affected by spherical aberration.

Spherical aberration correction with a spaceplate is performed in a fashion similar to that before: corrections to lateral ray positions in a manner that reduces spherical aberration translate to a desired spaceplate phase response as a function of incidence angle (upper inset, Figure 5d), which is used in the FoM for spaceplate optimization. Ray tracing and wave propagation simulations of the spherical lens−spaceplate system are summarized in Figure 5c,d. For normal incidence, the root-mean-square spot size calculated from the wave simulation, normalized by intensity, dropped from 2.17 μm without the spaceplate to 0.83 μm with the spaceplate. For off-axis illumination, the spherical aberration remains reduced. However, a new type of coma-like aberration is now clearly present, as visualized by the asymmetric ray distribution near the focal point. The introduction of coma due to the presence of the spaceplate corrector is fundamental to the translational symmetry properties of the spaceplate, and a more detailed analysis is in the Supporting Information. The ability of spaceplates to produce simultaneous responses to spherical and coma aberrations indicates that they may be ideally used as an aberration correction element in imaging systems featuring both types of aberrations.

■ CONCLUSIONS

In summary, we show that optical spaceplates can serve as multifunctional aberration correcting elements. Spaceplates are advantageous optical elements for aberration correction because they are translationally invariant, which simplifies alignment within an optical system, and they have a small footprint. Our design strategy is to cast aberration correction functionality as incident-angle- and wavelength-dependent lateral beam shifts, followed by the design of spaceplates around these figures of merits using an iterative gradient-based freeform optimization algorithm. With a series of benchmarks and demonstrations, we show that our design strategy can yield conventional spaceplates with best-in-class performance and aberration correcting spaceplates configured for chromatic, Petzval field curvature, and spherical aberrations. We anticipate these spaceplates to enhance imaging and metrology optical systems and that their beam shifting capabilities will also have applications in display technologies, optical computing, and optical signal processing.

We envision multiple avenues for future work. One direction is to codesign spaceplates with refractive optics to enable further enhanced aberration correction capabilities. These concepts can include individual or multiple refractive elements, and they can target the boosted correction of an individual aberration type or the correction of multiple aberration types. We anticipate this thrust to catalyze the development of multiscalar systems-level modeling and design tools that combine differential ray tracing with the TMM. Another direction is to understand how breaking the translational symmetry of spaceplates can lead to optical elements that combine space compression, aberration correction, polarization functionality, and wavefront shaping capabilities. Experimentally, grayscale optical spaceplates can be fabricated using multimaterial thin-film deposition and codeposition methods, and binary spaceplates can be fabricated simply using the alternating deposition of two material types.[39,40] For longer wavelength spaceplates, additive manufacturing can be used to print composite materials with tailored dielectric constant,[41] providing a route toward high-contrast grayscale devices.

■ ASSOCIATED CONTENT

SI Supporting Information

The Supporting Information is available free of charge at https://pubs.acs.org/doi/10.1021/acsphotonics.4c00086.

> Derivation of the lateral shift amount of thin-film multilayer structure, perturbation analysis, more detailed data for chromatic aberration correction with spaceplates, simulation method, method for co-optimization of spaceplate and aspheric lens for Petzval field curvature correction, discussion of aberration correction with spaceplates, and refractive index curve of BK7 glass (PDF)
>
> Structural details of several spaceplates presented in the paper (XLSX)

■ AUTHOR INFORMATION

Corresponding Author

Jonathan A. Fan − *Department of Electrical Engineering, Stanford University, Stanford, California 94305, United States;* orcid.org/0000-0001-9816-9979;
Email: jonfan@stanford.edu

Authors

Yixuan Shao − *Department of Electrical Engineering, Stanford University, Stanford, California 94305, United States;* orcid.org/0009-0009-6130-2831
Robert Lupoiu − *Department of Electrical Engineering, Stanford University, Stanford, California 94305, United States;* orcid.org/0000-0003-1649-2305
Jiaqi Jiang − *Department of Electrical Engineering, Stanford University, Stanford, California 94305, United States;* orcid.org/0000-0001-7502-0872
You Zhou − *Department of Electrical Engineering, Stanford University, Stanford, California 94305, United States;* orcid.org/0000-0002-5810-2347
Tom D. Milster − *James C. Wyant College of Optical Sciences, The University of Arizona, Tucson, Arizona 85721, United States*

Complete contact information is available at:
https://pubs.acs.org/10.1021/acsphotonics.4c00086

Notes

The authors declare no competing financial interest.

■ ACKNOWLEDGMENTS

This work was supported by the National Aeronautics and Space Administration under award no. 80NSSC21K0220 and the Office of Naval Research under Award Number N00014-20-1-2105. R.L. acknowledges support from the Knight Hennessey Fellowship. The authors thank E. Wollack of NASA for helpful discussions and feedback.

■ REFERENCES

(1) Shastri, K.; Reshef, O.; Boyd, R. W.; Lundeen, J. S.; Monticone, F. To what extent can space be compressed? Bandwidth limits of spaceplates. *Optica* **2022**, *9*, 738−745.

(2) Yu, N.; Capasso, F. Flat optics with designer metasurfaces. *Nat. Mater.* **2014**, *13*, 139−150.

(3) Arbabi, A.; Horie, Y.; Ball, A. J.; Bagheri, M.; Faraon, A. Subwavelength-thick lenses with high numerical apertures and large efficiency based on high-contrast transmitarrays. *Nat. Commun.* **2015**, *6*, 7069.

(4) Khorasaninejad, M.; Chen, W. T.; Devlin, R. C.; Oh, J.; Zhu, A. Y.; Capasso, F. Metalenses at visible wavelengths: Diffraction-limited focusing and subwavelength resolution imaging. *Science* **2016**, *352*, 1190−1194.

(5) Groever, B.; Chen, W. T.; Capasso, F. Meta-lens doublet in the visible region. *Nano Lett.* **2017**, *17*, 4902−4907.

(6) Phan, T.; Sell, D.; Wang, E. W.; Doshay, S.; Edee, K.; Yang, J.; Fan, J. A. High-efficiency, large-area, topology-optimized metasurfaces. *Light: Sci. Appl.* **2019**, *8*, 48.

(7) Zou, X.; Zheng, G.; Yuan, Q.; Zang, W.; Chen, R.; Li, T.; Li, L.; Wang, S.; Wang, Z.; Zhu, S. Imaging based on metalenses. *PhotoniX* **2020**, *1*, 2−24.

(8) Pan, M.; Fu, Y.; Zheng, M.; Chen, H.; Zang, Y.; Duan, H.; Li, Q.; Qiu, M.; Hu, Y. Dielectric metalens for miniaturized imaging systems: progress and challenges. *Light: Sci. Appl.* **2022**, *11*, 195.

(9) Zhou, Y.; Guo, S.; Overvig, A. C.; Alù, A. Multiresonant Nonlocal Metasurfaces. *Nano Lett.* **2023**, *23*, 6768−6775.

(10) Ossiander, M.; Meretska, M. L.; Hampel, H. K.; Lim, S. W. D.; Knefz, N.; Jauk, T.; Capasso, F.; Schultze, M. Extreme ultraviolet metalens by vacuum guiding. *Science* **2023**, *380*, 59−63.

(11) Khorasaninejad, M.; Chen, W. T.; Zhu, A. Y.; Oh, J.; Devlin, R. C.; Rousso, D.; Capasso, F. Multispectral Chiral Imaging with a Metalens. *Nano Lett.* **2016**, *16*, 4595−4600.

(12) Zhou, Y.; Kravchenko, I. I.; Wang, H.; Zheng, H.; Gu, G.; Valentine, J. Multifunctional metaoptics based on bilayer metasurfaces. *Light: Sci. Appl.* **2019**, *8*, 80.

(13) Hua, X.; Wang, Y.; Wang, S.; Zou, X.; Zhou, Y.; Li, L.; Yan, F.; Cao, X.; Xiao, S.; Tsai, D. P.; et al. Ultra-compact snapshot spectral light-field imaging. *Nat. Commun.* **2022**, *13*, 2732.

(14) Zou, X.; Zhang, Y.; Lin, R.; Gong, G.; Wang, S.; Zhu, S.; Wang, Z. Pixel-level Bayer-type colour router based on metasurfaces. *Nat. Commun.* **2022**, *13*, 3288.

(15) Arbabi, A.; Horie, Y.; Bagheri, M.; Faraon, A. Dielectric metasurfaces for complete control of phase and polarization with subwavelength spatial resolution and high transmission. *Nat. Nanotechnol.* **2015**, *10*, 937−943.

(16) Wu, P. C.; Tsai, W.-Y.; Chen, W. T.; Huang, Y.-W.; Chen, T.-Y.; Chen, J.-W.; Liao, C. Y.; Chu, C. H.; Sun, G.; Tsai, D. P. Versatile polarization generation with an aluminum plasmonic metasurface. *Nano Lett.* **2017**, *17*, 445−452.

(17) Rubin, N. A.; D'Aversa, G.; Chevalier, P.; Shi, Z.; Chen, W. T.; Capasso, F. Matrix Fourier optics enables a compact full-Stokes polarization camera. *Science* **2019**, *365*, No. eaax1839.

(18) Wang, E. W.; Phan, T.; Yu, S.-J.; Dhuey, S.; Fan, J. A. Dynamic circular birefringence response with fractured geometric phase metasurface systems. *Proc. Natl. Acad. Sci. U.S.A.* **2022**, *119*, No. e2122085119.

(19) Guo, C.; Wang, H.; Fan, S. Squeeze free space with nonlocal flat optics. *Optica* **2020**, *7*, 1133−1138.

(20) Reshef, O.; DelMastro, M. P.; Bearne, K. K.; Alhulaymi, A. H.; Giner, L.; Boyd, R. W.; Lundeen, J. S. An optic to replace space and its application towards ultra-thin imaging systems. *Nat. Commun.* **2021**, *12*, 3512.

(21) Chen, A.; Monticone, F. Dielectric nonlocal metasurfaces for fully solid-state ultrathin optical systems. *ACS Photonics* **2021**, *8*, 1439−1447.

(22) Mrnka, M.; Hendry, E.; Láčík, J.; Lennon, R. A.; Barr, L. E.; Hooper, I.; Phillips, D. B. Space squeezing optics: Performance limits and implementation at microwave frequencies. *APL Photonics* **2022**, *7*, 076105.

(23) Pagé, J. T. R.; Reshef, O.; Boyd, R. W.; Lundeen, J. S. Designing high-performance propagation-compressing spaceplates using thin-film multilayer stacks. *Opt. Express* **2022**, *30*, 2197−2205.

(24) Pahlevaninezhad, M.; Monticone, F. Multi-Color Spaceplates in the Visible. **2023**, arXiv:2312.02378v1 [physics.optics].

(25) Wang, S.; Wu, P. C.; Su, V.-C.; Lai, Y.-C.; Hung Chu, C.; Chen, J.-W.; Lu, S.-H.; Chen, J.; Xu, B.; Kuan, C.-H.; et al. Broadband achromatic optical metasurface devices. *Nat. Commun.* **2017**, *8*, 187.

(26) Chen, W. T.; Zhu, A. Y.; Sanjeev, V.; Khorasaninejad, M.; Shi, Z.; Lee, E.; Capasso, F. A broadband achromatic metalens for focusing and imaging in the visible. *Nature Nanotechnol.* **2018**, *13*, 220−226.

(27) Wang, S.; Wu, P. C.; Su, V.-C.; Lai, Y.-C.; Chen, M.-K.; Kuo, H. Y.; Chen, B. H.; Chen, Y. H.; Huang, T.-T.; Wang, J.-H.; et al. A broadband achromatic metalens in the visible. *Nature Nanotechnol.* **2018**, *13*, 227−232.

(28) Lin, R. J.; Su, V.-C.; Wang, S.; Chen, M. K.; Chung, T. L.; Chen, Y. H.; Kuo, H. Y.; Chen, J.-W.; Chen, J.; Huang, Y.-T.; et al. Achromatic metalens array for full-colour light-field imaging. *Nature Nanotechnol.* **2019**, *14*, 227−231.

(29) Chen, W. T.; Zhu, A. Y.; Sisler, J.; Bharwani, Z.; Capasso, F. A broadband achromatic polarization-insensitive metalens consisting of anisotropic nanostructures. *Nat. Commun.* **2019**, *10*, 355.

(30) Chung, H.; Miller, O. D. High-NA achromatic metalenses by inverse design. *Opt. Express* **2020**, *28*, 6945−6965.

(31) Shrestha, S.; Overvig, A.; Lu, M.; Stein, A.; Yu, N. Multi-element metasurface system for imaging in the near-infrared. *Appl. Phys. Lett.* **2023**, *122*, 201701.

(32) Avayu, O.; Almeida, E.; Prior, Y.; Ellenbogen, T. Composite functional metasurfaces for multispectral achromatic optics. *Nat. Commun.* **2017**, *8*, 14992.

(33) Arbabi, E.; Arbabi, A.; Kamali, S. M.; Horie, Y.; Faraji-Dana, M.; Faraon, A. MEMS-tunable dielectric metasurface lens. *Nat. Commun.* **2018**, *9*, 812.

(34) Zhou, Y.; Kravchenko, I. I.; Wang, H.; Nolen, J. R.; Gu, G.; Valentine, J. Multilayer noninteracting dielectric metasurfaces for multiwavelength metaoptics. *Nano Lett.* **2018**, *18*, 7529−7537.

(35) Miller, D. A. Why optics needs thickness. *Science* **2023**, *379*, 41−45.

(36) Nocedal, J.; Wright, S. J. *Numerical Optimization*; Springer, 1999.

(37) Luce, A.; Mahdavi, A.; Marquardt, F.; Wankerl, H. TMM-Fast, a transfer matrix computation package for multilayer thin-film optimization: tutorial. *J. Opt. Soc. Am. A* **2022**, *39*, 1007−1013.

(38) Yesilyurt, O.; Peana, S.; Mkhitaryan, V.; Pagadala, K.; Shalaev, V. M.; Kildishev, A. V.; Boltasseva, A. Fabrication-conscious neural network based inverse design of single-material variable-index multilayer films. *Nanophotonics* **2023**, *12*, 993−1006.

(39) Martin, P. M. *Handbook of Deposition Technologies for Films and Coatings: Science, Applications and Technology*; William Andrew, 2009.

(40) Jilani, A.; Abdel-Wahab, M. S.; Hammad, A. H. Advance deposition techniques for thin film and coating. In *Modern Technologies for Creating the Thin-film Systems and Coatings*; IntechOpen, 2017; Vol. 2, pp 137−149.

(41) Huang, Q.; Gan, L. T.; Fan, J. A. Conformal Volumetric Grayscale Metamaterials. *Adv. Mater.* **2023**, *35*, 2204688.